



Computational Discovery and Experimental Demonstration of Boron Phosphide Ultraviolet Nanoresonators

Svendsen, Mark K.; Sugimoto, Hiroshi; Assadillayev, Artyom; Shima, Daisuke; Fujii, Minoru; Thygesen, Kristian S.; Raza, Søren

Published in:
Advanced Optical Materials

Link to article, DOI:
[10.1002/adom.202200422](https://doi.org/10.1002/adom.202200422)

Publication date:
2022

Document Version
Publisher's PDF, also known as Version of record

[Link back to DTU Orbit](#)

Citation (APA):
Svendsen, M. K., Sugimoto, H., Assadillayev, A., Shima, D., Fujii, M., Thygesen, K. S., & Raza, S. (2022). Computational Discovery and Experimental Demonstration of Boron Phosphide Ultraviolet Nanoresonators. *Advanced Optical Materials*, 10(16), Article 2200422. <https://doi.org/10.1002/adom.202200422>

General rights

Copyright and moral rights for the publications made accessible in the public portal are retained by the authors and/or other copyright owners and it is a condition of accessing publications that users recognise and abide by the legal requirements associated with these rights.

- Users may download and print one copy of any publication from the public portal for the purpose of private study or research.
- You may not further distribute the material or use it for any profit-making activity or commercial gain
- You may freely distribute the URL identifying the publication in the public portal

If you believe that this document breaches copyright please contact us providing details, and we will remove access to the work immediately and investigate your claim.

Computational Discovery and Experimental Demonstration of Boron Phosphide Ultraviolet Nanoresonators

Mark K. Svendsen, Hiroshi Sugimoto, Artyom Assadillayev, Daisuke Shima, Minoru Fujii, Kristian S. Thygesen,* and Søren Raza*

Controlling ultraviolet light at the nanoscale using optical Mie resonances holds great promise for a diverse set of applications, such as lithography, sterilization, and biospectroscopy. Access to the ultraviolet requires materials with a high refractive index and wide band gap energy. Here, the authors systematically search for such materials by computing the frequency-dependent optical permittivity of 338 binary semiconductors and insulators from first principles, and evaluate their scattering properties using Mie theory. This analysis reveals several interesting candidate materials among which boron phosphide (BP) appears most promising. Then BP nanoparticles are prepared and it is demonstrated that they support Mie resonances at visible and ultraviolet wavelengths using both far-field optical measurements and near-field electron energy-loss spectroscopy. A laser reshaping method is also presented to realize spherical Mie-resonant BP nanoparticles. With a refractive index over three and low absorption losses in a broad spectral range spanning from the infrared to the near ultraviolet, BP is an appealing material for a broad range of applications in dielectric nanophotonics.

resonances have been realized at visible and infrared wavelengths thanks to the mature lithographic processing of suitable materials,^[4] such as silicon (Si),^[5] gallium phosphide (GaP),^[6] and titanium dioxide (TiO₂).^[7] It would be desirable to extend the operation of these materials to the ultraviolet, but their small direct band gap energies ($\lesssim 3$ eV) lead to significant absorption losses in the ultraviolet. Wide band gap materials, such as niobium pentoxide^[8] and hafnium oxide,^[9] offer transparency in the ultraviolet but at the cost of a moderate refractive index ($n \approx 2.1$ – 2.3). Diamond has been theoretically suggested as a potential material,^[10,11] but comes with significant nanofabrication challenges.^[12] The scarcity of available high-index materials with wide band gap energies calls for the identification of new materials which can advance the rich optical properties of Mie resonances observed in the visible to the ultraviolet.

1. Introduction

Achieving control over ultraviolet light with nanoscale materials is essential for improving surface-enhanced spectroscopies of biological molecules and enabling new ultraviolet optical components.^[1] Geometric Mie resonances supported by resonant nanoantennas made from materials that combine a high refractive index with low absorption losses offer efficient and tunable manipulation of the near- and far-field of optical waves.^[2,3] Mie

Concurrent advances in first-principles methodology and computing power have recently made it possible to design and discover new materials via high-throughput computations.^[13–17] The approach has been successfully applied in several domains, including photovoltaics, transparent conductors, and photocatalysis.^[18–20] However, to the best of our knowledge, computational discovery of new high-index materials remains largely unexplored. Relevant previous work in this direction has been limited to the static response regime^[21,22] reflecting the fact that the major materials databases so far has focused on ground state properties.

Here we use high-throughput linear response density functional theory (DFT) to screen an initial set of 2743 elementary and binary materials with the aim to identify isotropic high-index, low loss, and broad band optical materials. For the most promising materials, the computed frequency-dependent complex refractive indices are used as input for Mie scattering calculations to evaluate their optical performance. In addition to the already known high-index materials we identify several new compounds. In particular, boron phosphide (BP) offers a refractive index above three with very low absorption losses in a spectral range spanning from the infrared to the ultraviolet. We then prepare BP nanoparticles and show, by means of dark-field optical measurements and electron energy-loss spectroscopy, that they support size-dependent Mie resonances in the visible and ultraviolet. Finally, we demonstrate a laser reshaping

M. K. Svendsen, A. Assadillayev, K. S. Thygesen, S. Raza

Department of Physics

Technical University of Denmark, Fysikvej

Kongens Lyngby DK-2800, Denmark

E-mail: thygesen@fysik.dtu.dk; sraz@dtu.dk

H. Sugimoto, D. Shima, M. Fujii

Department of Electrical and Electronic Engineering

Kobe University

Rokkodai, Nada, Kobe 657-8501, Japan

 The ORCID identification number(s) for the author(s) of this article can be found under <https://doi.org/10.1002/adom.202200422>.

© 2022 The Authors. Advanced Optical Materials published by Wiley-VCH GmbH. This is an open access article under the terms of the Creative Commons Attribution License, which permits use, distribution and reproduction in any medium, provided the original work is properly cited.

DOI: 10.1002/adom.202200422

method to realize spherical BP nanoparticles, which host multiple Mie resonances in agreement with full-field optical simulations. Our experimental measurements demonstrate the potential of high-index BP across a broad spectral range as well as validate the refractive index obtained from DFT calculations. Besides the discovery of BP, we believe that our high-throughput screening provide an overview of existing materials as well as a pathway for realizing new high-index materials.

2. Results

2.1. High-Throughput Screening

Our high-throughput screening procedure is illustrated in Figure 1a. We build the workflow using the Python-based Atomic Simulation Recipes^[23] framework and the MyQueue scheduling software^[24] (see detailed workflow in Note S1 and Figure S1, Supporting Information). Starting from 2743 thermodynamically stable elementary and binary materials from the Open Quantum Materials Database^[15] we extract the 1693 materials with up to ten atoms in the unit cell and relax the atomic structure using DFT with the Perdew–Burke–Ernzerhof (PBE) exchange correlation functional^[25] and the D3 correction to account for the van der Waals forces.^[26] We perform DFT ground state calculations for all of the materials to determine their electronic band gaps. After discarding the metals, we are left with 338 semiconductors for which we calculate the optical dielectric function, $\epsilon(\omega)$, within the random phase approximation (RPA) and extract the refractive index and extinction coefficient as $n(\omega) = \text{Re}\{\sqrt{\epsilon(\omega)}\}$ and $k(\omega) = \text{Im}\{\sqrt{\epsilon(\omega)}\}$, respectively. All calculations are performed with the GPAW electronic structure code.^[27,28]

Next, we classify the materials according to the anisotropy of their refractive index tensor using a cut-off of 0.05 for the fractional anisotropy (see Figure S2, Supporting Information). This leaves us with 207 isotropic material candidates, for which we show the static refractive index as a function of the direct band gap in Figure 1b. In the Supporting Information, we provide refractive indices and band gap energies for all of the 207 material candidates. The data points qualitatively follow the Moss formula^[29] (dashed line in Figure 1b); however, there are significant deviations from the general trend, which we ascribe to variations in oscillator strength and density of the transitions across the direct gap. It is well known that (semi)local functionals like the PBE employed in the present work systematically underestimates band gaps.^[30] This effect is, however, to some extent compensated by the fact that the RPA neglects the attractive electron–hole interactions and consequently underestimates the spectral weight near the band edge. As a result, refractive indices obtained with RPA@PBE are typically in good agreement with experiments in the static limit^[28] while deviations occur at higher frequencies near the band edge region (see Note S2 and Figures S3–S5, Supporting Information). In Section 2.2, we will employ more accurate and computationally expensive many-body perturbation methods for the materials that are identified as interesting based on this screening.

We now turn to a more in-depth evaluation of the performance of the discovered materials. Specifically, we use Mie

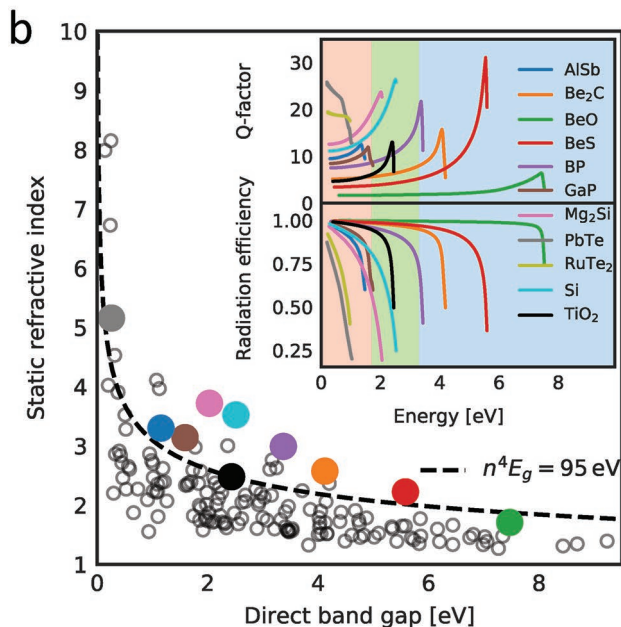
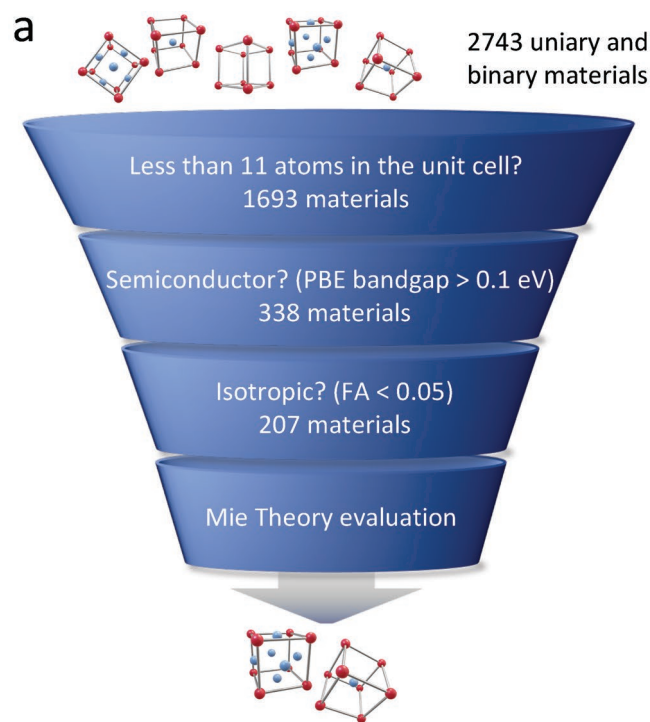


Figure 1. High-throughput materials screening. a) Schematic of the screening steps and the number of materials that survive each of them. b) The static refractive index of the isotropic materials plotted as a function of their direct band gap energies along with the Moss formula. The colored dots highlight interesting materials and the inset shows the energy-dependent Q -factor and radiation efficiency, η , of the MD resonances in those materials. The background colors represent the infrared (red), visible (green), and ultraviolet (blue) spectral regions.

theory to calculate the scattering properties of a spherical nanoparticle made from the subset of isotropic materials. We focus on the lowest-order magnetic dipole (MD) resonance of the spheres and calculate energy-dependent quality factors, Q , and

radiation efficiencies, η (see Note S1, Supporting Information).^[4] This is achieved by continuously adjusting the size of the sphere to tune the energy of the MD resonance across the infrared, visible, and ultraviolet regions. A high Q -factor is beneficial for boosting the local field enhancement of the nanoparticle, while radiation efficiency close to unity points to low absorption losses. This analysis identifies all of the commonly used materials, such as Si, TiO₂, and GaP. However, we also find a number of other highly promising materials, some of which are highlighted in the inset of Figure 1b. In particular, we identify BP, which has a refractive index exceeding that of TiO₂ and a radiation efficiency higher than both Si and TiO₂ across the entire visible part of the spectrum. For these reasons, we believe BP stands out as an overlooked material with highly desirable optical properties and we will focus on BP in the rest of the paper.

2.2. Optical Response of BP

BP crystals were successfully synthesized as early as 1957,^[31] yet experimental measurements of its refractive index are limited to a couple of data points in the visible.^[32,33] Refractive index measurements of BP thin films have also been conducted but with varying results.^[34,35]

The RPA@PBE permittivities used for the initial screening are qualitatively accurate but suffer from underestimated band gaps and missing excitonic effects. To determine the refractive index of BP with quantitative accuracy, we solve the Bethe–Salpeter equation (BSE) to obtain the permittivity using single-particle transition energies obtained from a G_0W_0 band structure calculation. The band structure calculation reveals an indirect band gap of 2.1 eV and a direct band gap of 4.41 eV, which matches experimental measurements of the band gap energies for BP.^[36,37] The square root dependence of the refractive index on the permittivity makes it crucial to converge both the real and imaginary parts of the latter. Unfortunately, the real part converges slowly with the number of bands making it impractical to obtain well converged results directly from the BSE. The problem can be alleviated by extending the imaginary part of the permittivity by an exponentially decaying tail whose weight is fixed by the f -sum rule (see Section 4), and subsequently obtain the real part via the Kramers–Kronig relation. We benchmark this approach against experimental data for the refractive index of crystalline Si and find excellent agreement (see Note S3 and Figure S6, Supporting Information).

With the f -sum rule fulfilling BSE- G_0W_0 method at hand, we are in a position to make a quantitative comparison of the refractive index of BP with some of the commonly used materials^[38,39] in the visible as well as diamond,^[40] which has been theoretically suggested for operation in the ultraviolet (Figure 2a,b). We observe that the absorption edge of BP lies significantly higher than Si, GaP, and TiO₂, while it retains a refractive index comparable to that of GaP. This suggests that BP provides low-loss operation across the entire visible spectrum and in the infrared (see Figure S7, Supporting Information). While this is also the case for TiO₂, its refractive index is significantly lower than that of BP. The higher refractive index of BP means that nanostructures can be made more compact^[41] and packed more densely for enhanced metasurface performance.^[42] Importantly, we

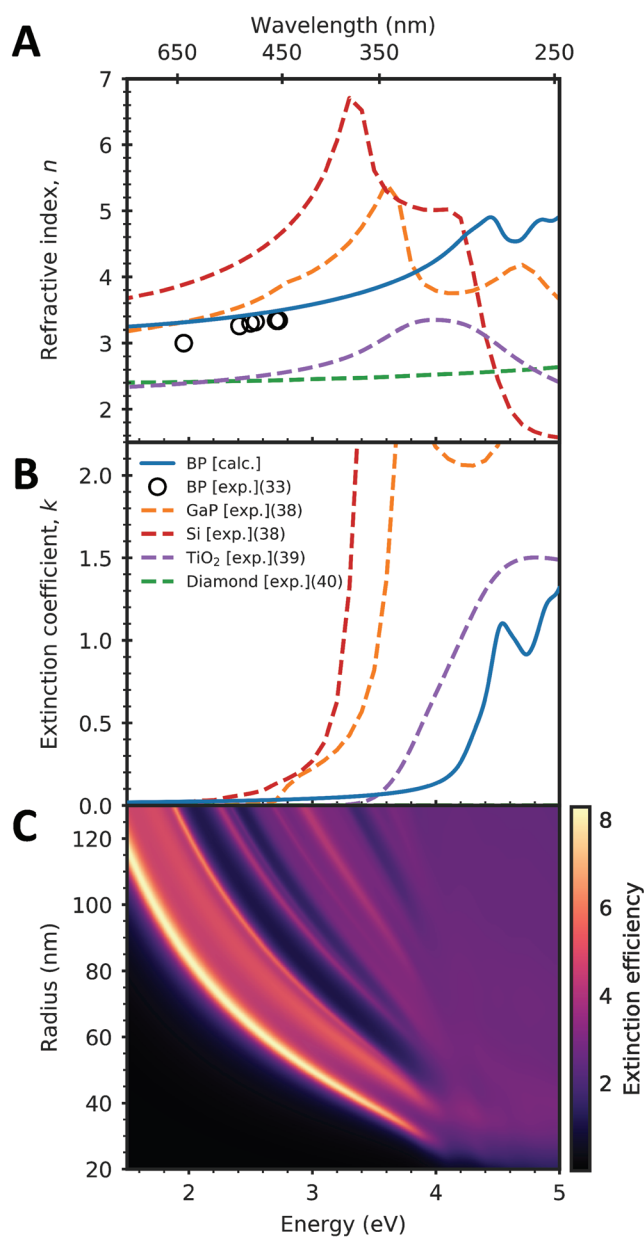


Figure 2. Optical response and Mie resonances of BP. a,b) Refractive index n and extinction coefficient k of BP calculated using the f -sum corrected BSE method compared with that of some of the commonly used dielectrics in the visible and ultraviolet spectral regions. c) Extinction efficiency map of BP spheres of varying radii calculated using Mie theory, which demonstrates that Mie resonances can be sustained in the visible and ultraviolet.

note that BP offers a high refractive index with a low extinction coefficient not only in the visible but also in the ultraviolet—a spectral region which is difficult to reach with the commonly used materials. Diamond is transparent in the ultraviolet as well, but has a significantly lower refractive index. We illustrate the broadband performance of BP by performing extinction efficiency calculations using Mie theory for a BP sphere with varying radii, confirming that Mie resonances can be sustained across the visible and ultraviolet (Figure 2c).

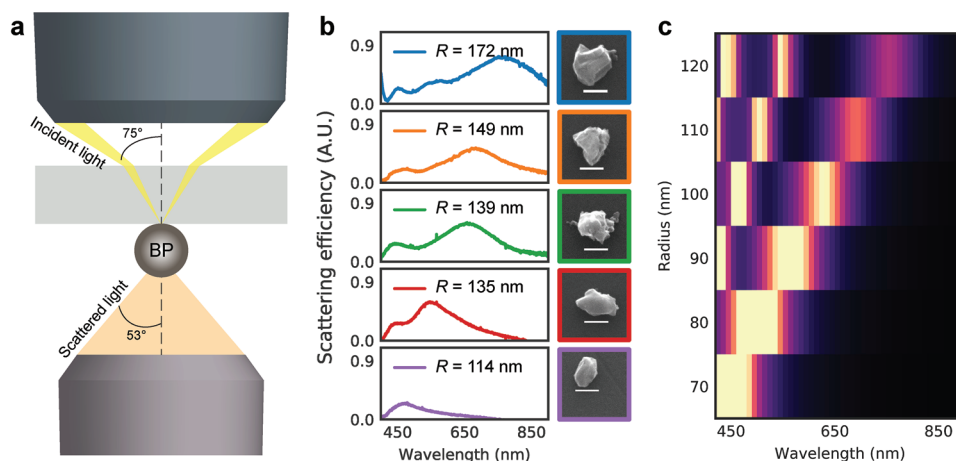


Figure 3. Dark-field scattering of BP nanoparticles. a) Schematic of the dark-field scattering spectroscopy. The nanoparticles are excited by unpolarized, white light incident at an oblique angle and the transmitted scattered light is collected. b) Scattering efficiency spectra recorded from individual BP nanoparticles of different sizes showing clear scattering peaks due to resonant interaction. The effective radius R of the nanoparticle is determined from the area of the particles, assuming a spherical shape. Scale bars: 200 nm. c) Simulated scattering efficiency map of BP nanospheres with varying particle radii.

2.3. Far- and Near-Field Characterization of BP Nanoparticles

We now turn to an experimental demonstration of the potential of BP as a Mie-resonant nanostructure. BP has been synthesized in various forms such as crystals,^[43,44] films,^[35,45–47] and nanoparticles.^[48–50] However, BP nanoparticles in the size range suitable for sustaining Mie resonances have not been reported. We prepare BP nanoparticles in the size range of a few hundred nanometers by grinding BP powder (Kojundo Chemicals) in a mortar and then dispersing it in methanol. The BP solution is subsequently dropcasted on a glass substrate.

We measure the far-field scattering efficiency of individual nanoparticles by illuminating the nanoparticles through a high-numerical-aperture dark-field objective and collecting the transmitted scattered light (see **Figure 3a**). A similar measurement setup has been used to detect Mie resonances in Si nanoparticles.^[51] The scattering spectra recorded from a series of BP nanoparticles clearly show resonant peaks, which red shift with increasing particle size (Figure 3b). Despite the irregular particle shapes, the scattering resonances are quite prominent and follow the trend observed in other Mie-resonant nanostructures, namely, that the smallest particle size support only the lowest-order Mie resonance while larger particle sizes also support higher-order Mie resonances.^[52] We additionally confirm the crystallinity of the nanoparticles using micro-Raman spectroscopy from individual nanoparticles (see Figure S8, Supporting Information). The particle radii are extracted from the scanning electron microscopy images under the assumption of a spherical shape and used as input for full-field simulations of the scattering efficiency of a BP nanosphere. The simulations account for the measurement setup as well as the glass substrate (see Section 4). We find that the simulations accurately reproduce both the shift in resonance wavelengths with particle size as well as the number of resonant peaks (Figure 3c). However, the particle sizes need to be adjusted to match the resonance wavelengths observed in the experiments. This suggests that the particle shape is better characterized as flakes

with a thickness significantly smaller than the in-plane size. Nonetheless, the distinctive, multiple scattering peaks provide strong evidence for the interpretation that these are related to geometric Mie resonances.

To gain more insight into the nature of these resonances and to access the ultraviolet spectral region, we also perform near-field characterization on similar BP nanoparticles using electron energy-loss spectroscopy (EELS). EELS is performed in a transmission electron microscope and has been employed to access near-field properties of both metallic^[53,54] and dielectric nanostructures^[55–57] as well as optical devices.^[58] The combined high spatial and spectral resolution of EELS provides unique nanoscale information on optical modes over a broad spectral range. For EELS measurements, the BP nanoparticles are deposited on a thin silicon dioxide membrane. The EELS signal recorded from a triangular-shaped BP nanoparticle (**Figure 4a**) at different beam positions is presented in Figure 4c. The position of the beam is directly related to the excitation efficiency of the optical modes,^[59] and thus, by judicious positioning of the beam we can selectively excite different Mie modes.^[55] When the beam is positioned in the center of nanoparticle, we observe a distinct resonance in the ultraviolet at 3.99 eV. As the beam is moved closer to the surface of the nanoparticle, two additional resonances are observed at the energies 3.57 and 2.77 eV. To identify the nature of these resonances, we simulate the EELS signal of a BP nanodisk with the same effective radius as the measured BP nanoparticle (Figure 4b). The thickness of the nanodisk is varied to achieve correspondence to the measured EELS resonance energies. The simulated EELS spectra for a nanodisk thickness of $h = 40$ nm at the same beam positions as in the experiments are shown in Figure 4d. Here, we observe that the three lowest-energy EELS peaks have the same dependence on the impact parameter of the electron beam as seen experimentally. The simulated resonance energies of all three EELS peaks are also in quantitative agreement with the experiments, albeit the lowest-energy EELS peak is slightly shifted to higher energies in the simulations. The measured EELS peaks

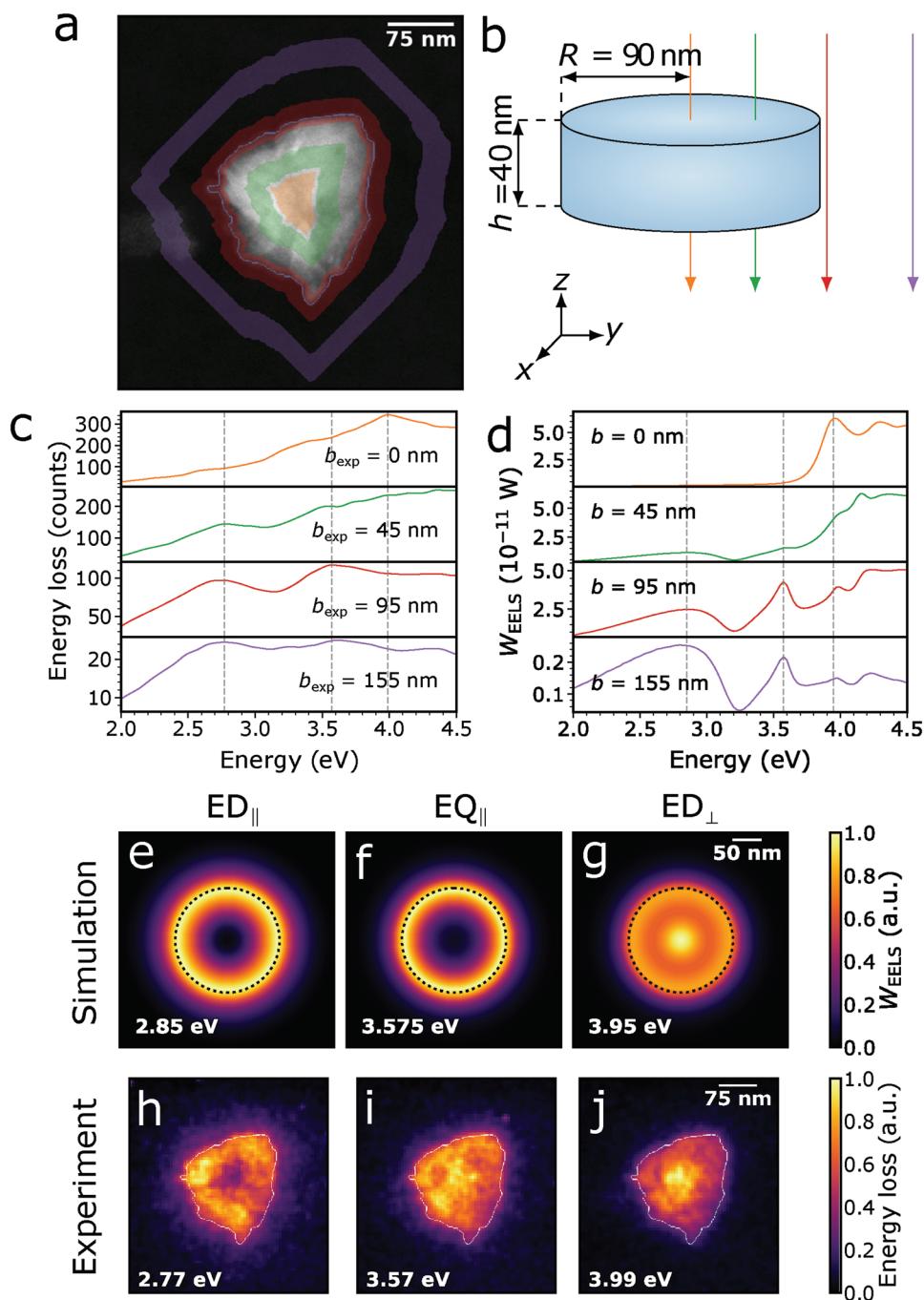


Figure 4. Electron energy-loss spectroscopy of BP nanoparticles. a,b) Experimental transmission electron microscopy image and theoretical set-up depicting the electron beam positions b used to acquire the measured and simulated EELS spectra of (c,d), respectively. The triangular-shaped BP nanoparticle is characterized by an effective radius of $R = 90$ nm. Several EELS peaks due to Mie resonances are observed. e–g) Simulated and h–j) experimental EELS intensity maps at the Mie resonance energies. The Mie modes are identified as the in-plane electric dipole (ED_{\parallel}), in-plane electric quadrupole (EQ_{\parallel}), and out-of-plane electric dipole (ED_{\perp}) using a multipole decomposition.

are broadened by the finite energy resolution of our EELS setup (see Section 4). By performing a multipole decomposition of the induced field produced by the electron beam,^[60] we identify the two lowest energy EELS peaks to be due to the Mie modes of the in-plane electric dipole ED_{\parallel} and in-plane electric quadrupole EQ_{\parallel} . The highest energy EELS peak has contributions

from both the in-plane magnetic dipole and out-of-plane electric dipole ED_{\perp} , where the latter dominates in the center of the particle (see Figure S9, Supporting Information for full decomposition). Simulated EELS intensity maps show that the electron beam couples efficiently to the in-plane modes, ED_{\parallel} and EQ_{\parallel} , for beam positions near the surface of the particle, while the

out-of-plane ED_{\perp} is excited also for beam positions in the center of the particle (Figure 4e–g). The experimental EELS intensity maps (Figure 4h–j) of these three Mie modes are in good agreement with the simulations as well as previous EELS measurements performed on Mie-resonant Si nanoparticles.^[55,56]

The dark-field scattering measurements (Figure 3) combined with the EELS measurements (Figure 4) show that the optically resonant nature of the BP nanoparticles can be identified both in their far-field and near-field responses, respectively. These resonances are present both in the visible and ultraviolet and their resonance energies can be tuned with particle size. The insight from both of these measurement techniques reveals that, despite their irregular shape, BP nanoparticles host a variety of multipolar Mie resonances, which are key attributes of low-loss high-index nanostructures.

2.4. Laser Reshaping

To alleviate the irregular shape of the as-prepared BP nanoparticles, we generate spherical BP nanoparticles by irradiating the unprocessed BP nanoparticles with a pulsed laser (see Figure 5a and Section 4). An example of a laser-processed BP nanoparticle is presented in Figure 5b, confirming that the laser processing can be used for realizing spherical-shaped BP nanoparticles without affecting the nanoparticle composition. In addition, we perform micro-Raman spectroscopy on the same particle and find that the crystallinity from the unprocessed BP nanoparticles is retained after laser reshaping (see Figure S8, Supporting Information). The dark-field scattering spectrum from the BP nanoparticle in Figure 5b is recorded and we observe multiple scattering peaks (Figure 5c). The relatively large particle radius ($R = 184$ nm) places the lowest-order Mie resonances at wavelengths longer than our measurement range, while the scattering peaks observed can be attributed to higher-order Mie resonances. The full-field simulation of a BP nanosphere with a slightly smaller radius $R = 165$ nm, where we account for the substrate and the measurement setup, shows very good agreement with the measurement. We attribute the deviation in particle radius to shape imperfections and a slight variation between the calculated and experimental refractive index of BP. Multipole decomposition reveals that the scattering peaks are due to the excitation of the magnetic quadrupole (MQ), the electric quadrupole (EQ), and radial higher-order magnetic dipole (MD^2), thereby confirming the Mie-resonant nature of BP nanoparticles. We also performed EELS measurements on a smaller laser-reshaped BP nanoparticle, where we observe Mie resonances in the ultraviolet (see Figure S10, Supporting Information).

3. Conclusion

Using a DFT-based high-throughput screening method combined with optical Mie theory of 338 dielectrics, we identify BP as a promising high-refractive-index material for ultraviolet nanooptics. We develop a new, quantitatively accurate many-body perturbation theory based methodology for calculating refractive indices and use it to reveal that BP has a high refractive index ($n > 3$) and low extinction coefficient ($k < 0.1$) up to

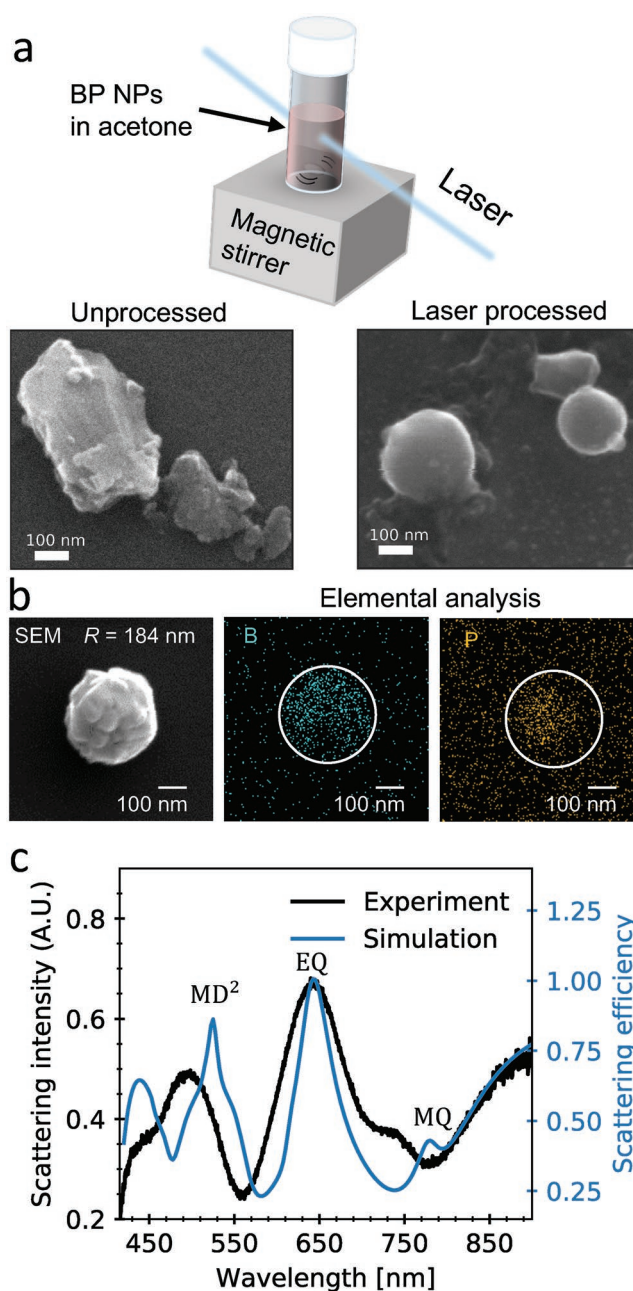


Figure 5. Laser reshaping of BP nanoparticles. a) Reshaping of the BP nanoparticles is achieved by pulsed laser irradiation of unprocessed BP nanoparticles in acetone. After the irradiation, the BP nanoparticles obtain a spherical shape. b) Scanning electron microscopy image and energy-dispersive X-ray analysis of reshaped BP nanoparticle, showing a spherical shape without change in composition. c) Scattering spectrum recorded from the BP nanoparticle in (b) and simulated spectrum for a BP nanosphere with radius $R = 165$ nm with multipole decomposition revealing the excitation of the magnetic quadrupole (MQ), electric quadrupole (EQ), and radial higher-order magnetic dipole (MD^2).

ultraviolet photon energies of 4 eV. We present an approach to fabricate BP nanoparticles as well as a laser reshaping method to generate spherical BP nanoparticles. Through dark-field optical spectroscopy and EELS measurements, we confirm the

presence of Mie resonances in BP nanoparticles across the visible and ultraviolet. Our work advances nanoscale Mie optics to the ultraviolet and may find applications in metasurface-enhanced spectroscopy of biological molecules and, more generally, in realizing metasurface optical components operating in the ultraviolet.

4. Experimental Section

Structural Relaxation: All ground- and excited state calculations were performed with the GPAW electronic structure code.^[27] The atomic structure and the unit cell of the materials were relaxed until the maximum force (stress) is below 10^{-4} eV Å⁻¹ (0.002 eV Å⁻³). The PBE functional for exchange and correlation effects, a Γ -point centered k -point grid with a density of 6.0Å^{-3} , a 800 eV plane wave cutoff, and a Fermi-Dirac smearing of 50 meV was used. van der Waals interactions were taken into account by the D3 correction scheme.^[26]

RPA Calculations: The optical permittivity, $\epsilon(\omega)$, was calculated within the RPA using the dielectric function module in GPAW. From $\epsilon(\omega)$ the refractive index and extinction coefficient were calculated as $n(\omega) = \text{Re}\{\sqrt{\epsilon(\omega)}\}$ and $k(\omega) = \text{Im}\{\sqrt{\epsilon(\omega)}\}$, respectively. To ensure convergence across all materials a k -point grid with a high density of 20.0Å^{-3} was employed and conduction bands up to five times the number of valence bands were included. The calculations were performed on a nonlinear frequency grid with an initial frequency spacing of 0.5 meV, a broadening of 50 meV, and a local field cutoff of 50 eV.

G₀W₀ Calculations: The G₀W₀ calculations were performed on top of the ground state calculations. To ensure converged quasi-particle gaps extrapolation of both the plane wave cut-off and the k -point resolution to infinity were performed.

BSE Calculations: The BSE calculations were performed within the Tamm–Dancoff approximation on a k -point grid with a density of 20Å^{-3} . The calculation included all valence and conduction bands within 2.3 eV of the valence band maximum and conduction band minimum, respectively. The calculation of the screened interaction included all occupied bands and unoccupied bands up to five times the number of occupied bands, and local field effects were accounted for up to a plane wave cut-off of 50 eV. The calculation was performed on a linear 10 001 point frequency grid spanning 0–8 eV.

BSE f -Sum Rule Correction: The optical polarizability has to obey the f -sum rule

$$\int_0^\infty d\omega \omega \text{Im}\chi(\omega) = \frac{\pi}{2} \frac{n_e e^2}{m} \quad (1)$$

where n_e is the electron density, e is the elementary charge, and m is the electron mass. Since it is not obvious what to use for n_e in the PAW calculations, a different strategy was used to fix the left hand side, namely, it was obtained from an RPA calculation (which can be readily converged)

$$\int_0^\infty d\omega \omega \text{Im}\chi^{(\text{RPA})}(\omega) = \int_0^\infty d\omega \omega \text{Im}\chi^{(\text{BSE})}(\omega) \quad (2)$$

Equation (2) can be enforced if the imaginary part of the BSE polarizability was artificially extended. Denoting the largest transition energy included in the BSE calculation as ω_c , the following extension was performed

$$\text{Im}\chi^{(\text{BSE})}(\omega) = \begin{cases} \text{Im}\chi^{(\text{BSE})}(\omega), & \text{if } \omega \leq \omega_c \\ C_0 e^{-\gamma(\omega-\omega_c)}, & \text{if } \omega > \omega_c \end{cases} \quad (3)$$

The constant C_0 is used to ensure continuity and the constant γ is fixed to give the correct spectral weight as fixed by Equation (2). For benchmarks and additional details see Supporting Information.

Optical Simulations: The scattering efficiency and EELS simulations were both performed in COMSOL Multiphysics (version 5.6), which solves Maxwell's equations using finite-element modeling. For the scattering efficiency simulations in Figure 3c, a BP sphere is placed on a semi-infinite glass substrate ($n_{\text{sub}} = 1.45$) and excited by a plane wave incident from the substrate side at an oblique angle of $\theta_{\text{inc}} = 42^\circ$. The f -sum corrected refractive index was used for BP shown in Figure 2. Then a near-to-far field transformation was performed to extract the scattered far-field.^[61] The Poynting flux of the scattered far-field in the air region was integrated over a solid angle spanning an azimuthal angle of 2π and a maximum polar angle of $\theta_{\text{col}} = \arcsin(\text{NA}) = 53^\circ$ to retrieve the total scattered power collected by the collection objective (NA = 0.8). The total scattered power was normalized to the incident power and the geometrical cross sectional area of the particle to determine the scattering efficiency. To account for the unpolarized incident light in the experiments, this simulation procedure was performed for both transverse-electric and transverse-magnetic polarization of the incident wave. Finally, the scattering efficiency from both polarization states was averaged. The scattering efficiency simulation in Figure 5c followed the same steps with the only change being that the plane wave was incident from the air side at an oblique angle of $\theta_{\text{inc}} = 75^\circ$.

For the EELS calculations, the electron beam was simulated as an edge current with an amplitude of $1\ \mu\text{A}$. The induced electromagnetic field was obtained by calculating the fields with and without the BP nanodisk in the simulation domain, and subsequently subtracting them. The energy loss was then calculated as the work rate done on the electron beam by the induced electromagnetic field.^[55]

Dark-Field Scattering Measurements: A custom-built inverted optical microscope was used for dark-field scattering spectroscopy of single nanoparticles (Figure 3a). For the measurements presented in Figure 3, the sample is illuminated from the top by a halogen lamp through a dark field condenser and the scattered light was collected by an objective (50 \times , NA = 0.8). For the spectrum in Figure 5c, the sample was illuminated from the bottom through a dark-field objective (50 \times , NA = 0.8) and the scattered light was collected by the same objective. To measure the spectra, scattered light was transferred to the entrance slit of a monochromator (SpectraPro-300i, Princeton Instruments) and detected by a liquid-N₂ cooled CCD (Princeton Instruments). For Raman scattering measurements, the nanoparticles were excited by a 488 nm laser (Coherent Sapphire 488–50).

EELS Measurements and Analysis: The EELS measurements were performed in a monochromated and aberration-corrected FEI Titan operated in STEM mode at an acceleration voltage of 300 kV, providing a probe size of ≈ 0.5 nm and an energy resolution of 0.08 eV (as measured by the full-width-at-half-maximum of the zero-loss peak). Richardson–Lucy deconvolution was performed to remove the zero-loss peak. An EELS spectrum recorded in vacuum was used as an input for the point-spread function. Due to a small asymmetry in the zero-loss peak, the deconvolution algorithm produced an artificial EELS peak in the energy range below 0.5 eV. However, the artificial peak did not overlap with any of the observed resonances and could be safely removed using a first-order logarithmic polynomial.

The depicted EELS spectra were obtained by integrating the deconvoluted EELS data around the experimental impact parameter b_{exp} . This parameter was directly related to the effective radius of the particle R which was extracted as a radius of the circle with the effective area of the particle found from the STEM image. The effective area of the particle is the area which was enclosed by the boundaries obtained by Otsu's thresholding of the STEM image. The integration parameter itself was calculated as a radius of the circle with the adjusted effective area of expanded/reduced initial boundaries. For the integration region centered at the nanoparticle, the experimental impact parameter changes from 0 to $0.3R$ and denotes the nanoparticle center. For the annulus-shaped regions, the experimental impact parameter denoted the mean of the inner and outer radii with a typical radius spread of 0.3 (for example, the green region in Figure 4a encloses the regions from 0.35 to $0.65R$). The depicted EELS spectra were smoothed with a Gaussian function ($\sigma = 0.03$ eV).

The EELS maps were obtained by summing the deconvoluted EELS data in a spectral window of 0.02 eV width centered at the resonance energies. The signal-to-noise ratio was improved by spatially binning the map, reducing the total number of pixels by a factor of four. A Gaussian filter with $\sigma = 0.8$ pixels was applied to smooth the image.

Laser Reshaping: The laser reshaping was performed using a laser melting in liquid process.^[62,63] The process yields spherical nanoparticles from irregular shaped nanoparticles by selective heating due to the light absorption of solid particles. Unprocessed BP nanoparticles in acetone were irradiated with the third harmonic of a Nd:YAG laser (355 nm wavelength, 5 nm pulse width, 20 Hz repetition rate) with a fluence of 50 mJ cm⁻² per pulse for 10 min to obtain spherical BP nanoparticles.

Supporting Information

Supporting Information is available from the Wiley Online Library or from the author.

Acknowledgements

S.R. and A.A. acknowledge support from the Independent Research Funding Denmark (7026-00117B). K.S.T. acknowledges support from the Center for Nanostructured Graphene (CNG) under the Danish National Research Foundation (project DNR103) and from the European Research Council (ERC) under the European Union's Horizon 2020 research and innovation program (Grant No. 773122, LIMA). K.S.T. is a Villum Investigator supported by VILLUM FONDEN (Grant No. 37789). H.S. acknowledges support by JSPS KAKENHI Grant Number 21K14496.

Conflict of Interest

The authors declare no conflict of interest.

Author Contributions

M.K.S. constructed the computational workflow, performed the screening, developed the f-sum approach, and prepared the figures. H.S. performed the structural and optical characterizations of nanoparticles. A.A. performed the EELS measurements, EELS analysis, EELS simulations, and prepared a figure. D.S. fabricated the nanoparticles and conducted laser shaping processes. M.F. contributed to analyses and interpretation of the data and supervised the fabrication and characterizations of nanoparticles. S.R. and K.S.T. conceived the idea and supervised the work. S.R. performed the optical simulations. All authors discussed the results and contributed to the preparation of the manuscript.

Data Availability Statement

The data that support the findings of this study are available from the corresponding author upon reasonable request.

Keywords

boron phosphide, electron energy-loss spectroscopy, high-refractive-index nanostructures, high-throughput screening, laser reshaping, Mie resonances

Received: February 22, 2022

Revised: April 1, 2022

Published online: May 29, 2022

- [1] D. Zhao, Z. Lin, W. Zhu, H. J. Lezec, T. Xu, A. Agrawal, C. Zhang, K. Huang, *Nanophotonics* **2021**, *10*, 2283.
- [2] A. I. Kuznetsov, A. E. Miroshnichenko, M. L. Brongersma, Y. S. Kivshar, B. Luk'yanchuk, *Science* **2016**, *354*, aag2472.
- [3] S. Kruk, Y. Kivshar, *ACS Photonics* **2017**, *4*, 2638.
- [4] D. G. Baranov, D. A. Zuev, S. I. Lepeshov, O. V. Kotov, A. E. Krasnok, A. B. Evlyukhin, B. N. Chichkov, *Optica* **2017**, *4*, 814.
- [5] I. Staude, J. Schilling, *Nat. Photonics* **2017**, *11*, 274.
- [6] D. J. Wilson, K. Schneider, S. Hönl, M. Anderson, Y. Baumgartner, L. Czornomaz, T. J. Kippenberg, P. Seidler, *Nat. Photonics* **2020**, *14*, 57.
- [7] W. T. Chen, A. Y. Zhu, V. Sanjeev, M. Khorasaninejad, Z. Shi, E. Lee, F. Capasso, *Nat. Nanotechnol.* **2018**, *13*, 220.
- [8] K. Huang, J. Deng, H. S. Leong, S. L. K. Yap, R. B. Yang, J. Teng, H. Liu, *Laser Photon. Rev.* **2019**, *13*, 1800289.
- [9] C. Zhang, S. Divitt, Q. Fan, W. Zhu, A. Agrawal, Y. Lu, T. Xu, H. J. Lezec, *Light Sci. Appl.* **2020**, *9*, 55.
- [10] Y. Gutiérrez, D. Ortiz, J. M. Saiz, F. González, P. Albella, F. Moreno, *Appl. Sci.* **2018**, *8*, 2065.
- [11] J. Hu, M. Lawrence, J. A. Dionne, *ACS Photonics* **2020**, *7*, 36.
- [12] I. Aharonovich, A. D. Greentree, S. Praver, *Nat. Photonics* **2011**, *5*, 397.
- [13] S. Curtarolo, G. L. Hart, M. B. Nardelli, N. Mingo, S. Sanvito, O. Levy, *Nat. Mater.* **2013**, *12*, 191.
- [14] A. Jain, S. P. Ong, G. Hautier, W. Chen, W. D. Richards, S. Dacek, S. Cholia, D. Gunter, D. Skinner, G. Ceder, K. A. Persson, *APL Mater.* **2013**, *1*, 011002.
- [15] S. Kirklin, J. E. Saal, B. Meredig, A. Thompson, J. W. Doak, M. Aykol, S. Rühl, C. Wolverton, *NPJ Comput. Mater.* **2015**, *1*, 15010.
- [16] S. Haastrup, M. Strange, M. Pandey, T. Deilmann, P. S. Schmidt, N. F. Hinsche, M. N. Gjerding, D. Torelli, P. M. Larsen, A. C. Riis-Jensen, J. Gath, K. W. Jacobsen, J. J. Mortensen, T. Olsen, K. S. Thygesen, *2D Mater.* **2018**, *5*, 042002.
- [17] M. N. Gjerding, A. Taghizadeh, A. Rasmussen, S. Ali, F. Bertoldo, T. Deilmann, N. R. Knøsgaard, M. Kruse, A. H. Larsen, S. Manti, T. G. Pedersen, U. Petralanda, T. Skovhus, M. K. Svendsen, J. J. Mortensen, T. Olsen, K. S. Thygesen, *2D Mater.* **2021**, *8*, 044002.
- [18] J. B. Varley, A. Miglio, V.-A. Ha, M. J. van Setten, G.-M. Rignanese, G. Hautier, *Chem. Mater.* **2017**, *29*, 2568.
- [19] L. Yu, A. Zunger, *Phys. Rev. Lett.* **2012**, *108*, 068701.
- [20] I. E. Castelli, T. Olsen, S. Datta, D. D. Landis, S. Dahl, K. S. Thygesen, K. W. Jacobsen, *Energy Environ. Sci.* **2012**, *5*, 5814.
- [21] I. Petousis, D. Mrdjenovich, E. Ballouz, M. Liu, D. Winston, W. Chen, T. Graf, T. D. Schladt, K. A. Persson, F. B. Prinz, *Sci. Data* **2017**, *4*, 160134.
- [22] F. Naccarato, F. Ricci, J. Suntivich, G. Hautier, L. Wirtz, G.-M. Rignanese, *Phys. Rev. Mater.* **2019**, *3*, 044602.
- [23] M. Gjerding, T. Skovhus, A. Rasmussen, F. Bertoldo, A. H. Larsen, J. J. Mortensen, K. S. Thygesen, *Comput. Mater. Sci.* **2021**, *199*, 110731.
- [24] J. J. Mortensen, M. Gjerding, K. S. Thygesen, *J. Open Source Software* **2020**, *5*, 1844.
- [25] J. P. Perdew, K. Burke, M. Ernzerhof, *Phys. Rev. Lett.* **1996**, *77*, 3865.
- [26] S. Grimme, J. Antony, S. Ehrlich, H. Krieg, *J. Chem. Phys.* **2010**, *132*, 154104.
- [27] J. Enkovaara, C. Rostgaard, J. J. Mortensen, J. Chen, M. Duřak, L. Ferrighi, J. Gavnholt, C. Glinsvad, V. Haikola, H. Hansen, H. H. Kristoffersen, M. Kuisma, A. H. Larsen, L. Lehtovaara, M. Ljungberg, O. Lopez-Acevedo, P. G. Moses, J. Ojanen, T. Olsen, V. Petzold, N. A. Romero, J. Stausholm-Møller, M. Strange, G. A. Tritsarlis, M. Vanin, M. Walter, B. Hammer, H. Häkkinen, G. K. H. Madsen, R. M. Nieminen, *J. Phys.: Condens. Matter* **2010**, *22*, 253202.
- [28] J. Yan, J. J. Mortensen, K. W. Jacobsen, K. S. Thygesen, *Phys. Rev. B* **2011**, *83*, 245122.
- [29] T. Moss, *Phys. Status Solidi B* **1985**, *131*, 415.
- [30] J. P. Perdew, *Int. J. Quantum Chem.* **1985**, *28*, 497.

- [31] P. Popper, T. A. Ingles, *Nature* **1957**, 179, 1075.
- [32] T. Takenaka, M. Takigawa, K. Shohno, *Jpn. J. Appl. Phys.* **1976**, 15, 2021.
- [33] W. Wettling, J. Windscheif, *Solid State Commun.* **1984**, 50, 33.
- [34] M. Odawara, T. Udagawa, G. Shimaoka, *Jpn. J. Appl. Phys.* **2005**, 44, 681.
- [35] S. Dalui, S. Hussain, S. Varma, D. Paramanik, A. K. Pal, *Thin Solid Films* **2008**, 516, 4958.
- [36] R. J. Archer, R. Y. Koyama, E. E. Loebner, R. C. Lucas, *Phys. Rev. Lett.* **1964**, 12, 538.
- [37] E. Schroten, A. Goossens, J. Schoonman, *J. Appl. Phys.* **1998**, 83, 1660.
- [38] D. E. Aspnes, A. Studna, *Phys. Rev. B* **1983**, 27, 985.
- [39] T. Siefke, S. Kroker, K. Pfeiffer, O. Puffky, K. Dietrich, D. Franta, I. Ohlidal, A. Szeghalmi, E.-B. Kley, A. Tünnermann, *Adv. Opt. Mater.* **2016**, 4, 1780.
- [40] H. Phillip, E. Taft, *Phys. Rev.* **1964**, 136, A1445.
- [41] J. Yang, J. A. Fan, *Opt. Express* **2017**, 25, 23899.
- [42] P. Lalanne, P. Chavel, *Laser Photonics Rev.* **2017**, 11, 1600295.
- [43] Y. Kumashiro, *J. Mater. Res.* **1990**, 5, 2933.
- [44] K. Woo, K. Lee, K. Kovnir, *Mater. Res. Express* **2016**, 3, 074003.
- [45] Y. Kumashiro, K. Nakamura, T. Enomoto, M. Tanaka, *J. Mater. Sci. Mater. Electron.* **2011**, 22, 966.
- [46] B. Padavala, C. D. Frye, X. Wang, Z. Ding, R. Chen, M. Dudley, B. Raghobhamachar, P. Lu, B. N. Flanders, J. H. Edgar, *Cryst. Growth Des.* **2016**, 16, 981.
- [47] A. Crovetto, J. M. Adamczyk, R. R. Schnepf, C. L. Perkins, H. Hempel, S. R. Bauers, E. S. Toberer, A. C. Tamboli, T. Unold, A. Zakutayev, *Adv. Mater. Interfaces* **2022**, 9, 2200031.
- [48] H. Sugimoto, M. Fujii, K. Imakita, *RSC Adv.* **2015**, 5, 8427.
- [49] M. Feng, J. Zhang, H. Zhou, P. Jiang, D. Zhang, L. Wang, S. Chen, *Mater. Res. Express* **2019**, 6, 125922.
- [50] H. Sugimoto, B. Somogyi, T. Nakamura, H. Zhou, Y. Ichihashi, S. Nishiyama, A. Gali, M. Fujii, *J. Phys. Chem. C* **2019**, 123, 23226.
- [51] H. Sugimoto, M. Fujii, *Adv. Opt. Mater.* **2017**, 5, 1700332.
- [52] H. Sugimoto, T. Okazaki, M. Fujii, *Adv. Opt. Mater.* **2020**, 8, 2000033.
- [53] F. J. García de Abajo, *Rev. Mod. Phys.* **2010**, 82, 209.
- [54] C. Colliex, M. Kociak, O. Stéphan, *Ultramicroscopy* **2016**, 162, A1.
- [55] A. Assadillayev, T. Hinamoto, M. Fujii, H. Sugimoto, M. L. Brongersma, S. Raza, *ACS Photonics* **2021**, 8, 1582.
- [56] A. Assadillayev, T. Hinamoto, M. Fujii, H. Sugimoto, S. Raza, *Nano-photonics* **2021**, 10, 4161.
- [57] D. T. Alexander, V. Flauraud, F. Demming-Janssen, *ACS Nano* **2021**, 15, 16501.
- [58] J. H. Song, S. Raza, J. van de Groep, J. H. Kang, Q. Li, P. G. Kik, M. L. Brongersma, *Nat. Commun.* **2021**, 12, 48.
- [59] S. Raza, M. Esfandyarpour, A. L. Koh, N. A. Mortensen, M. L. Brongersma, S. I. Bozhevolnyi, *Nat. Commun.* **2016**, 7, 13790.
- [60] R. Alaei, C. Rockstuhl, I. Fernandez-Corbaton, *Opt. Commun.* **2018**, 407, 17.
- [61] J. Yang, J. P. Hugonin, P. Lalanne, *ACS Photonics* **2016**, 3, 395.
- [62] X. Li, A. Pyatenko, Y. Shimizu, H. Wang, K. Koga, N. Koshizaki, *Langmuir* **2011**, 27, 5076.
- [63] D. Zhang, B. Gökce, S. Barcikowski, *Chem. Rev.* **2017**, 117, 3990.